Geophysical Journal International

Geophys. J. Int. (2010) **181,** 1539–1546 doi: 10.1111/j.1365-246X.2010.04584.x

FAST TRACK PAPER

Coseismic and initial post-seismic slip of the 2009 M_w 6.3 L'Aquila earthquake, Italy, from GPS measurements

D. Cheloni,[1] N. D'Agostino,[1] E. D'Anastasio,[1] A. Avallone,[1] S. Mantenuto,[2] R. Giuliani,[3] M. Mattone,[3] S. Calcaterra,[4] P. Gambino,[4] D. Dominici,[5] F. Radicioni[6] and G. Fastellini[6]

[1]*Istituto Nazionale di Geofisica e Vulcanologia, Centro Nazionale Terremoti, Roma, Italy. E-mail: nicola.dagostino@ingv.it*
[2]*Leica Geosystems, Roma, Italy*
[3]*Dipartimento Protezione Civile, Roma, Italy*
[4]*Istituto Superiore per la Protezione e la Ricerca Ambientale, Roma, Italy*
[5]*Dipartimento di Architettura e Urbanistica, Università degli Studi dell'Aquila, L'Aquila, Italy*
[6]*Dipartimento di Ingegneria Civile ed Ambientale, Università degli Studi di Perugia, Perugia, Italy*

Accepted 2010 March 2. Received 2010 January 27; in original form 2009 July 9

SUMMARY

Here we report the preliminary results of GPS data inversions for coseismic and initial afterslip distributions of the M_w 6.3 2009 April 6 L'Aquila earthquake. Coseismic displacements of continuous and survey-style GPS sites, show that the earthquake ruptured a planar SW-dipping normal fault with ∼0.6 m average slip and an estimated moment of 3.9×10^{18} Nm. Geodetic data agree with the seismological and geological information pointing out the Paganica fault, as the causative structure of the main shock. The position of the hypocentre relative to the coseismic slip distribution supports the seismological evidence of southeastward rupture directivity. These results also point out that the main coseismic asperity probably ended downdip of the Paganica village at a depth of few kilometres in agreement with the small (1–10 cm) observed surface breaks. Time-dependent post-seismic displacements have been modelled with an exponential function. The average value of the estimated characteristic times for near-field sites in the hanging-wall of the fault is 23.9 ± 5.4 d. The comparison between coseismic slip and post-seismic displacements for the first 60 d after the main shock, shows that afterslip occurred at the edges of the main coseismic asperity with a maximum estimated slip of ∼25 cm and an equivalent seismic moment of 6.5×10^{17} Nm. The activation of the Paganica fault, spatially intermediate between the previously recognized main active fault systems, suggests that strain accumulation in the central Apennines may be simultaneously active on distinct parallel fault systems.

Key words: Satellite geodesy; Earthquake source observations; Continental tectonics: extensional; Europe.

1 INTRODUCTION

The M_w 6.3 L'Aquila earthquake struck the Abruzzi region in central Italy (Fig. 1) on 2009 April 6 causing extensive damage to the town of L'Aquila and killing 300 inhabitants. The main shock nucleated at a depth of 8–10 km, was preceded by a pre-seismic sequence with the largest shock having a Ml 4 magnitude, and was followed by a vigorous aftershock sequence, primarily southeast and north of the hypocentre (Chiarabba *et al*. 2009). The normal faulting mechanism (Fig. 2) agrees with the NE–SW direction of active extension across the Apennines caused by the northeastward motion of the Adriatic microplate (D'Agostino *et al.* 2008). Previous geological studies (Boncio *et al.* 2004; Roberts & Michetti 2004; Galli *et al.* 2008) have recognized several NW–SE-trending fault systems active in the Upper Pleistocene–Holocene in this part of the Central Apennines. Preliminary geodetic investigations (D'Agostino *et al*. 2001; Mantenuto 2008) have suggested that strain accumulation is focused on the westernmost active fault system (Fig. 1) which from the High Aterno Valley joins the Ovindoli–Pezza–Fucino fault system with minor activity on the easternmost fault system. Immediately after the main shock we re-occupied survey-mode GPS benchmarks, retrieved data from continuous GPS stations and deployed new continuous GPS sites in the epicentral area. In this study, we use the GPS data to infer the fault geometry, the amount of coseismic slip

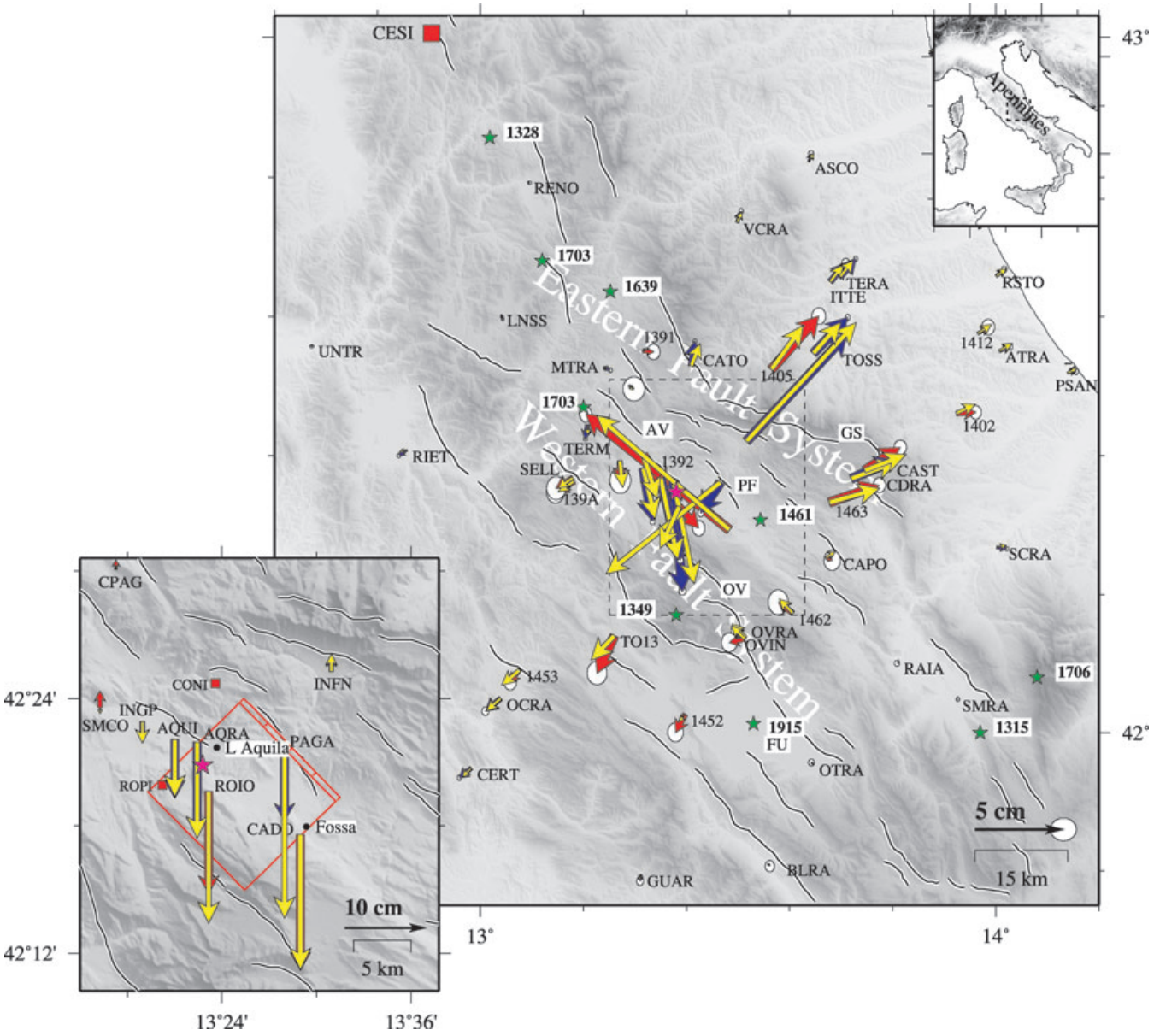

Figure 1. GPS coseismic displacements of the 2009 April 6th M_w 6.3 L'Aquila earthquake (pink star, epicentre; blue vectors, continuous GPS; red, survey-style GPS; yellow, uniform slip dislocation model; error ellipses at 95 per cent C.I.; green stars, $I_{max} > X$ historic earthquakes labelled with A.D. epoch). Black lines are active faults from Galli *et al.* (2008), Boncio *et al.* (2004) and Roberts & Michetti (2004). The red square indicates the position of the station CESI. The inset shows observed (blue) and calculated (yellow) vertical displacements. The red box in the inset is the surface projection of the best-fitting uniform slip fault model. The ticked line is where extension of the fault plane intersects the surface. Red squares in the inset indicate continuous GPS sites deployed after the main shock. Legend: AV, High Aterno Valley; GS, Gran Sasso range; PF, Paganica fault; OV, Ovindoli-Pezza fault; FU, Fucino.

and the initial post-seismic afterslip and we discuss the results in relation to the source and rupture geometry and their seismotectonic significance.

2 GPS DATA AND ANALYSIS

In this study, we use data from 36 permanent GPS sites (51 per cent within 50 km from the epicentre; Table S1) managed by different agencies. Two additional permanent GPS stations (ROPI, CONI) were installed within 2 d from the main shock. We included 14 survey-style GPS benchmarks (50 per cent within 26 km, the rest within 55 km from the epicentre). These sites have multiple years of pre-earthquake measurements (last in 2008) and well-established interseismic velocities (D'Agostino *et al*. 2001; Mantenuto 2008). The GPS benchmarks within 25 km from the epicentre have been immediately measured after the main shock (day of year 96–98) while the others were occupied within the following week. We also included five survey-mode sites described by Anzidei *et al.* (2009) installed 4 d before the main shock. Two of them (CADO, ROIO) were left to collect data continuously for post-seismic deformation.

We use the GIPSY-OASIS software to analyse GPS data using a precise-point-positioning strategy followed by network ambiguity resolution aligning daily solutions to ITRF2005 following the method described in D'Agostino *et al*. (2008). We mapped horizontal and vertical displacements with respect to the INGV (Istituto

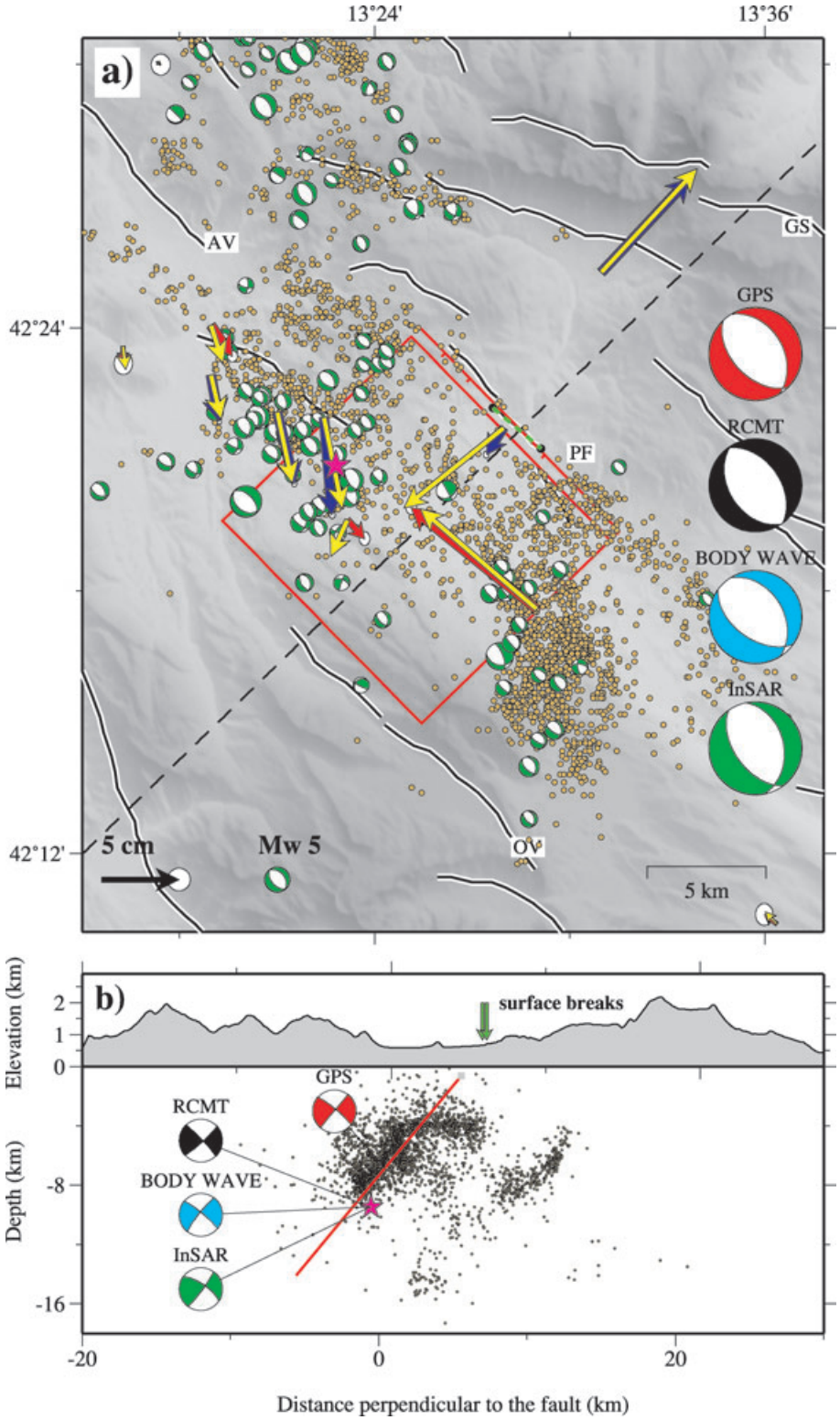

Figure 2. (a) Observed and calculated coseismic GPS displacements. Yellow circles are relocated aftershocks of the first 60 d after the main shock (Chiarabba *et al.* 2009). Large beach-balls represent regional CMT (Pondrelli *et al.* 2009), body-wave (Walters *et al.* 2009), InSAR (Walters *et al.* 2009) and GPS (this study) focal solutions. Small beach-balls are $M_w > 3$ moment tensor solutions available at http://www.eas.slu.edu/Earthquake_Center/MECH.IT. The dashed green line represents the extent of observed ground ruptures along the Paganica fault. (b) Relocated aftershocks and topographic cross-section.

Nazionale Geofisica Vulcanologia) station CESI (Fig. 1) to increase the signal-to-noise ratio of the position time-series relative to absolute position time-series expressed in a global reference frame. The CESI site (about 80 km northwest of the epicentre) do not show any evidence of coseismic offset and has a negligible secular motion relative to the stations near the epicentre (D'Agostino *et al.* 2008). To account for the interseismic motion that occurred at the survey sites without pre-earthquake measurements in the days before the

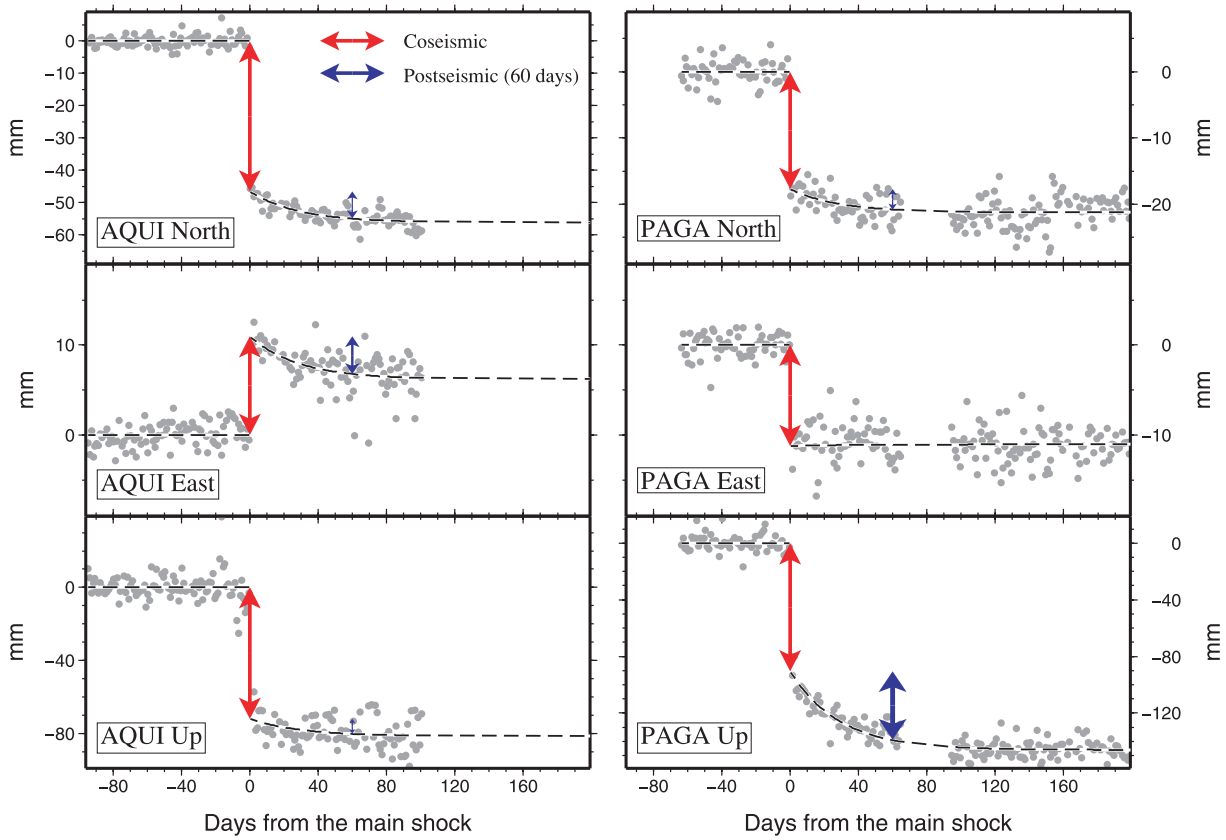

Figure 3. Time-series of PAGA and AQUI sites. The dashed line is the best-fitting exponential function (details in the main text). Arrows correspond to estimated coseismic offsets (red) and post-seismic cumulated displacements (blue).

earthquake, we estimate the positions just before the earthquake using the interseismic velocity with the uncertainty being propagated into the pre-earthquake position. Vertical offsets have been considered for permanent sites and for those survey sites, which maintained the same antenna setup across the main shock. Due to the daily sampling of the GPS time-series, our estimate of coseismic slip includes post-seismic afterslip of the first day. Permanent GPS sites show clear evidence of coseismic offset followed, for sites in the near-field, by a clear time-dependent post-seismic signal (Fig. 3 and Fig. S1). We modelled site positions as the sum of a coseismic offset and an exponential term representing the time-dependent post-seismic deformation. The model equation used to parametrize the time-dependent deformation is $v_i = y_i^0 + A_i H[t] + B_i[1 - \exp(-t/d_c)]H[t]$ where y_i^0 is the initial position, A_i is the coseismic offset for ith component, t is time after the earthquake, H is the Heaviside step function, B_i is an amplitude decay factor for the ith component, and d_c is a characteristic decay time. y_i^0, A_i and B_i are simultaneously estimated by linear least-squares while the parameter d_c (common to the north, east and vertical components) is found by iteratively minimizing the model misfit over a range of values. Although the data is well fit by this model, we do not ascribe a physical significance or predictive power to the estimated model parameters. For permanent sites installed after the earthquake we estimate the initial position y_i^0 and the time-dependent deformation parameters B_i, d_c. Survey sites without a sufficient number of post-seismic measurements were used to estimate y_i^0 and the coseismic offset A_i. We calculate the cumulative post-seismic displacements 60 d after the main shock formally propagating the data error (Tables S3–S6). The largest horizontal and vertical coseismic displacements reach 8.1 and 16.5 cm, respectively, as compared to 1.0 and 4.9 cm for the post-seismic ones. To verify that the largest aftershocks (M_w 5.5 April 7, M_w 5.4 April 9, Pondrelli *et al.* 2009) do not contribute significantly to the post-seismic deformation signal we modelled the surface offsets produced by equidimensional buried dislocations whose area is equivalent to the rupture area of a 3 MPa stress drop circular cracks. We also visually inspected the epoch-by-epoch 5 min position time-series (D'Anastasio *et al*. 2009) at the time of the shocks. In both cases we have not observed significant static offsets for $M_w > 5$ shocks other than the main shock.

3 FAULT GEOMETRY AND COSEISMIC SLIP

To infer the geometry of the uniform slip fault we model the observed near and far-field coseismic displacements, using a rectangular dislocation in an elastic, homogeneous and isotropic half-space (Okada 1985). Because the displacements are related nonlinearly to the nine parameters describing the geometry and the slip of the fault plane, we used a simulated annealing algorithm (Corana *et al*. 1987) to determine the model that produces the least-squares best fit. To estimate the confidence intervals we used a Monte Carlo simulation technique (e.g. Press *et al.* 1992) which applies the best-fitting technique to a large number of synthetic data sets, each one derived from adding synthetic realizations of data noise to the actual data set. The individual model parameters appear to be well resolved with compact 95 per cent confidence intervals. The most significant

parameter trade-offs are observed between strike and rake, north position and slip, and depth and dip of the fault (Fig. S2). The best-fitting uniform slip model (Fig. 2 and Table S7) is described by a 50° SW-dipping fault plane in good agreement with hypocentral location, distribution of aftershocks, seismological estimates of seismic moment and small surface ruptures (1–10 cm) observed near Paganica (Emergeo Working Group 2009; Falcucci *et al.* 2009). The average uniform slip is 0.6 m which (using a value of 30 GPa for rigidity) gives an estimated seismic moment of 3.9×10^{18} Nm.

Horizontal and vertical displacements (Figs 1 and 2) are generally well reproduced for the near and far-field sites (rms values in mm: 3.9 east, 3.3 north, 7.8 up) with the exception of the site PAGA located few hundreds metres from the surface emergence of the best-fitting fault model. Surface displacements at GPS sites located above the shallower part of the fault are most sensible to the fine slip distribution and may not be compatible with the uniform slip constrain imposed for the evaluation of the best-fitting fault geometry. The site PAGA has thus been excluded for the estimation of the best-fitting uniform slip fault. The AQRA and CADO sites provide strong constraints on the lateral edges of the uniform slip fault. A uniform slip model is able to reproduce most of the observed vertical and horizontal signals with the exception of the near-field sites ROIO and CADO, which cannot be fully reproduced with a uniform slip model.

To test variable slip on the fault plane we subdivided the uniform-slip fault in patches of 1×1 km and we computed Green's function relating slip on each patch to the 3-D displacements at GPS sites assuming an elastic half-space with a Poisson ratio of 0.25 and fixing the rake at the best-fitting uniform-slip model. We apply positivity constraints in order to avoid implausible and overly rough slip distribution and regularize the inversion by applying smoothing via a finite-difference approximation of the Laplacian operator with the balance between data misfit and fault slip smoothness controlled by factor k. We choose the amount of smoothing from a trade-off curve with misfit function plotted as a function of solution roughness (Fig. S4). The result shows only a marginal improvement in rms reduction (3.5 versus 5.1 mm) mostly accomplished by reduction in the vertical (4.6 versus 7.8 mm) misfit and slight reduction in the north (2.7 versus 3.3 mm) and in the east (2.6 versus 3.9 mm) misfits. A similar minor misfit improvement from a uniform to a variable slip models is also shown by inversion of InSAR data (Walters *et al*. 2009). The variable slip model shows three major asperities with ∼1 m of maximum slip, entirely contained within the uniform slip fault (Fig. 5) and remarkably consistent with the slip distribution obtained from the joint inversion of strong motion and GPS data by Cirella *et al.* (2009). The asperity with largest slip lies at a depth of 3–8 km downdip of the observed surface ruptures. Upward tapering of this asperity is consistent with the small-observed surface ruptures and fringes continuity of the InSAR interferograms (Atzori *et al*. 2009; Walters *et al*. 2009). The position of the main shock relative to the slip distribution (Fig. 4) supports the seismological inference of SE rupture directivity (Cirella *et al*. 2009; Pino & Di Luccio 2009). Resolution tests have been performed (Figs S3a and S3b) showing limited resolution on slip in the deepest part of the fault (>10 km) which improves in the shallower parts.

4 AFTERSLIP INVERSION

We model initial post-seismic deformation as the result of afterslip on the fault using the cumulative post-seismic deformation calculated at the near-field sites 60 d after the main shock. A significant change (Fig. 4a,c) between the coseismic and post-seismic displacement patterns suggests that different parts of the fault moved as a consequence of the afterslip following the main shock. It can be observed that sites near L'Aquila (AQUI, AQRA and ROIO) distinctly inverted the sign of the coseismic east component in the post-seismic phase (Fig. 3 and Fig. S1). A change between coseismic and post-seismic deformation is also observed at site CADO which moved coseismically towards northwest and post-seismically towards northeast. It is interesting to remark that the time-dependent displacement fit to the stations on the hanging-wall of the fault (1392, AQRA, AQUI, CADO, INGP, PAGA and ROIO) provide similar results in terms of the characteristic decay time d_c with an average value of 23.9 ± 5.4 d suggesting that sites on the hanging-wall of the fault moved post-seismically in response to a common physical process. This value corresponds to approximately half of the motion of the first 60 d achieved in the first 15 d.

To model heterogeneous fault afterslip we use the same parametrization (fault length, rake, subfault patch dimension) of the variable coseismic slip inversion. Resolution tests show an improvement in the ability to resolve slip distribution on the fault both in the shallow and deep parts of the fault as a result of the larger number of available GPS data (Fig. S3c and S3d). Nevertheless it is possible that a significant amount of slip is not 'seen' by our GPS station distribution. Horizontal and vertical post-seismic displacements are well reproduced by a variable slip model with three main patches labelled with A, B and C in Fig. 5. Patch A, at a depth of approximately 15 km, is required by the southwestward motion and moderate downward displacements of the GPS sites near L'Aquila. Patch B correlates with several aftershocks and remains stable when PAGA is excluded from the inversion. The strongest constraint on patch B comes from the northward motion of CADO, which require upward tapering slip. Extending the slip upward to the surface in fact changes the horizontal motion of CADO by more than 90°. The very shallow (less than 3 km) patch C is required by the motion of CONI and by the horizontal displacements of the sites near L'Aquila, suggesting that the small surface ruptures (Emergeo Working Group 2009) may have here reached the surface or increased their offsets as a consequence of shallow afterslip.

The comparison with the coseismic slip distribution strongly suggests that afterslip of patches A and B was triggered at the edges of the largest coseismic asperities where gradients of slip determined significant increase of shear stress on the unruptured parts of the fault surface. We also observe that patches B and C correspond to those parts of the fault where Amoruso & Crescentini (2009) found significant afterslip using laser strainmeter data. In general we observe an inverse correlation of afterslip relative to the coseismic slip with shallow slip in the central and southeastern parts and deeper in the northwestern part of the fault.

5 DISCUSSION AND CONCLUSION

Our results show that the M_w 6.3 L'Aquila earthquake occurred on a 50°-dipping 136N-striking normal fault producing small (1–10 cm) ruptures along the surface trace of the Paganica fault which was previously considered as active in the Late Quaternary (Bagnaia *et al.* 1992) and in the Holocene (Boncio *et al.* 2004). Where the coseismic rupture reached the surface the Paganica fault presents a well-developed cumulative Quaternary fault scarp and a flat hanging-wall alluvial plain suggestive of periodic episodes of coseismic subsidence and repeated failure of the same asperity. The geodetic and

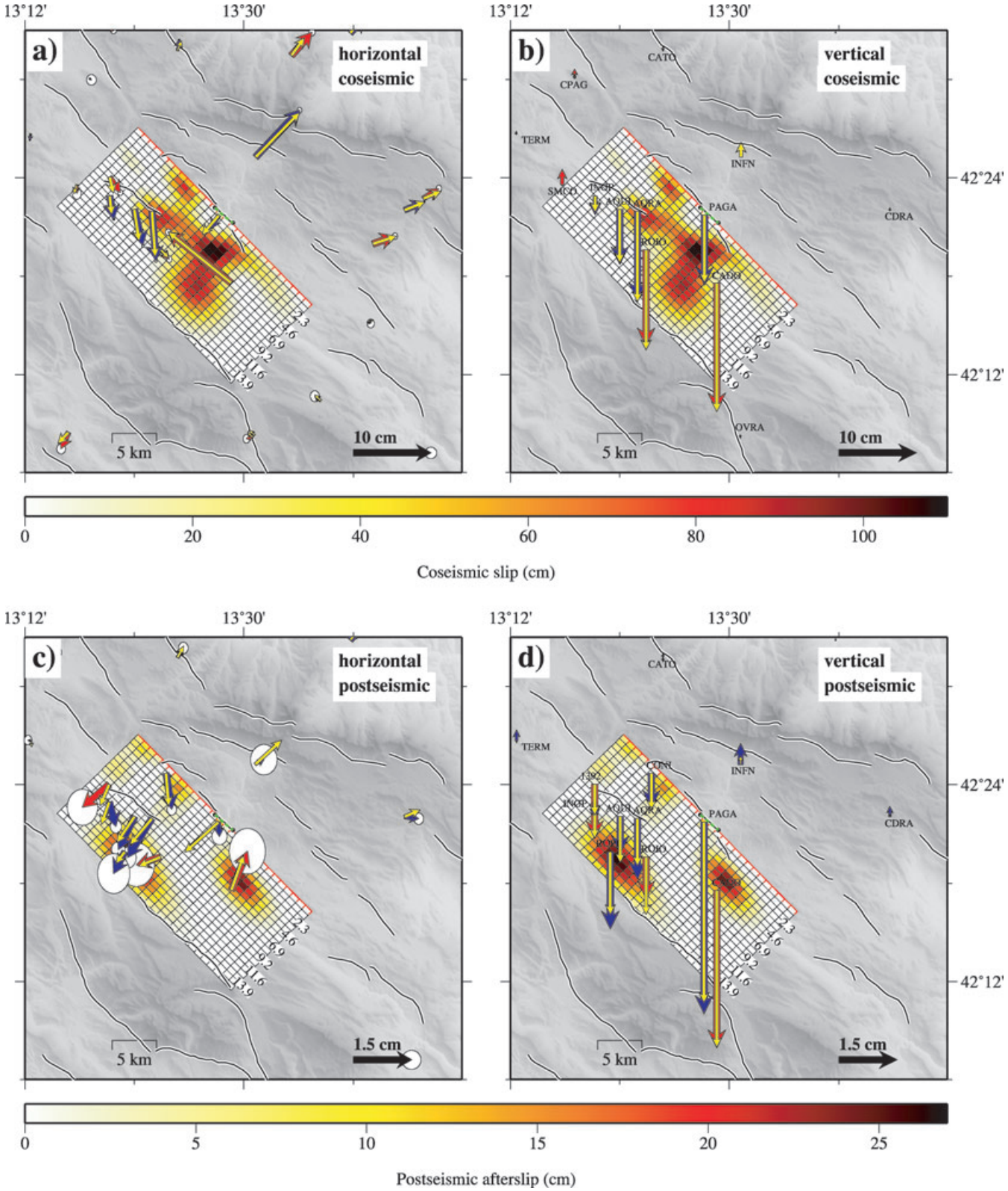

Figure 4. Coseismic slip distribution (a,b) and afterslip (c,d) estimated from cumulative 60-d post-seismic displacements (blue arrows, continuous GPS; red, survey-sites GPS; 95 per cent C.I. error ellipse; yellow, model predictions). Note the different colour scale for coseismic and post-seismic slip distributions.

seismological seismic moment estimates generally agree, suggesting that the largest part of the rupture radiated seismically and that geodetic estimates are not significantly biased by early post-seismic deformation. The position of the hypocentre relative to the entire fault plane is consistent with the seismological evidence of a strong southeastward rupture directivity. Inversion of GPS data yields a main asperity at a depth of about 3–7 km downdip of the observed surface breaks. The inversion of the post-seismic displacements

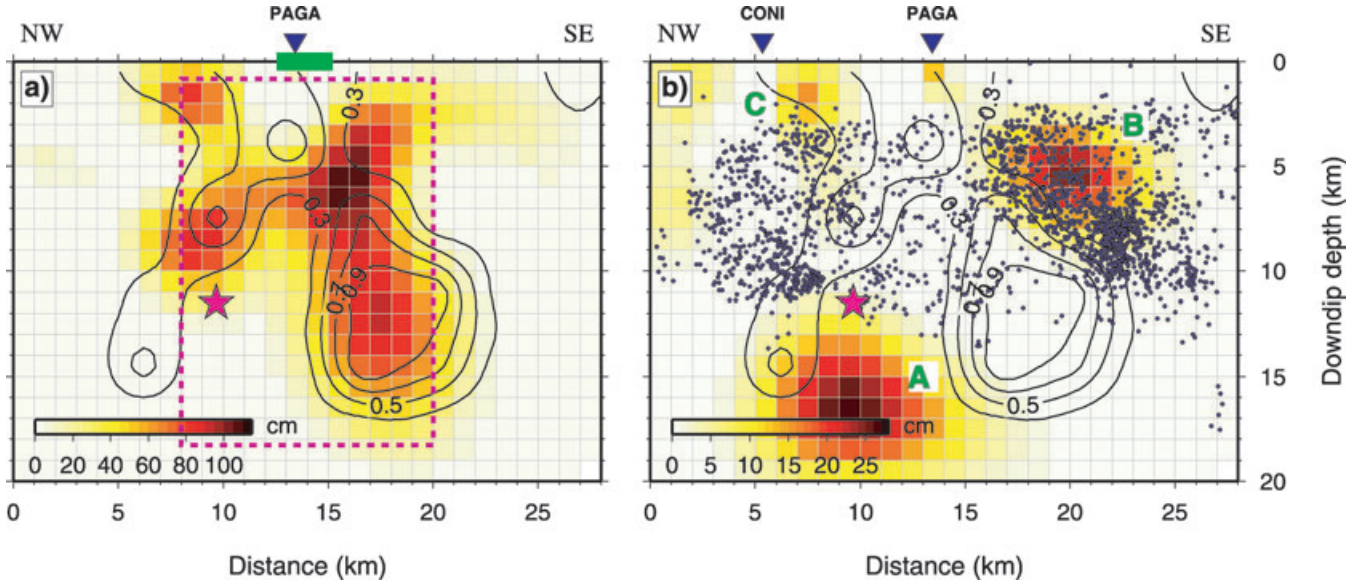

Figure 5. Comparison of coseismic slip (a) and afterslip (b) distributions. The pink dashed line in the coseismic plot is the best-fitting uniform slip model. The main afterslip patches in (b) are labelled with A, B and C and discussed in the text. The thick green line in (a) indicates the extent of surface breaks. The contours represent coseismic slip (spacing 0.2 m), estimated using both geodetic and strong motion data (Cirella *et al.* 2009). Earthquakes within 2 km are projected on the fault surface and shown as a pink star (main shock) or blue circles (relocated aftershocks). Note that afterlip and aftershocks concentrate at the edges of the larger coseismic slip patches.

shows that afterslip occurred at the edges of the main coseismic patches releasing, in the first 60 d after the main shock, a post-seismic moment of 6.5×10^{17} Nm, equivalent to a M_w 5.8 earthquake. The inverse correlation between coseismic slip and afterslip suggests that post-seismic deformation partly smoothed the coseismic slip distribution. The occurrence of the L'Aquila earthquake on the Paganica fault, intermediate between the two, previously recognized, main active fault systems (D'Agostino *et al*. 2001; Boncio *et al*. 2004; Galli *et al*. 2008), suggests that tectonic loading may be active across more than a single, dominant seismic belt, emphasizing the need for an improved geodetic investigation of interseismic strain accumulation in this part of the Apennines.

ACKNOWLEDGMENTS

We dedicate this work to Renato Funiciello who was the great and beloved teacher of many of us. We thank the INGV staff of Grottaminarda (in particular V. Cardinale, C. D'Ambrosio, A. Memmolo and F. Minichiello) for rapid post-seismic deployment of continuous GPS, and F. Criscuoli for survey-sites measurements, C. Chiarabba for the aftershock relocations and M. Anzidei for rinex files of the survey sites. We also thank Bill Hammond, an anonymous reviewer and the Associated Editor Falk Amelung for constructive observations, which helped to increase the quality of the manuscript.

REFERENCES

Amoruso, A. & Crescentini, L., 2009. Slow diffusive fault slip propagation following the 2009/04/06 L'Aquila earthquake, Italy, *Geophys. Res. Lett.,* **36,** L24306, doi:10.1029/2009GL041503.

Anzidei, M. *et al*., 2009. Coseismic deformation of the destructive April 6, 2009 L'Aquila earthquake (central Italy) from GPS data, *Geophys. Res. Lett.,* **36,** L17307, doi: 10.1029/2009GL039145.

Atzori, S. *et al*., 2009. Finite fault inversion of DInSAR coseismic displacement of the 2009 L'Aquila earthquake (Central Italy), *Geophys. Res. Lett.,* **36,** L15305, doi: 10.1029/2009GL039293.

Bagnaia, R., D'Epifanio, A. & Sylos Labini, S., 1992. Aquila and subaequan basins: an example of Quaternary evolution in Central Apennines, Italy, *Quarter. Nova,* **II,** 187–209.

Boncio, P., Lavecchia, G. & Pace, B., 2004. Defining a model of 3D seismogenic sources for Seismic Hazard Assessment applications: the case of central Apennines (Italy), *J. Seismol.,* **8,** 407–425.

Chiarabba *et al*. 2009. The 2009 L'Aquila (central Italy) Mw 6.3 earthquake: Mmain shock and aftershocks, *Geophys. Res. Lett.,* **36,** L18308, doi:10.1029/2009GL039627.

Cirella, A., Piatanesi, A., Cocco, M., Tinti, E., Scognamiglio, L., Michelini, A., Lomax, A. & Boschi, E., 2009. Rupture history of the 2009 L'Aquila earthquake from non-linear inversion of strong motion and GPS data, *Geophys. Res. Lett.,* **36,** L19304, doi:10.1029/2009GL039795.

Corana, A., Marchesi, M., Martini, C. & Ridella, S., 1987. Minimizing multimodal functions of countinuous variables with the "Simulated Annealing" algorithm, *ACM Trans. Math. Softw.,* **13,** 262–280.

D'Agostino, N., Avallone, A., Cheloni, D., D'Anastasio, E., Mantenuto, S. & Selvaggi, G., 2008. Active tectonics of the Adriatic region from GPS and earthquake slip vectors, *J. geophys. Res.,* **113,** B12413, doi:10.1029/2008JB005860.

D'Agostino, N., Giuliani, R., Mattone, M. & Bonci, L., 2001. Active Crustal Extension in the Central Apennines (Italy) Inferred from GPS Measurements in the Interval 1994–1999, *Geophys. Res. Lett.,* **28**(10), 2121–2124.

D'Anastasio, E., Blewitt, G., D'Agostino, N., Avallone, A., Cheloni, D. & Marzario, M., 2009. The 2009 L'Aquila Earthquake: Postseismic Deformation with High Temporal Resolution Using the new GPS "Carrier Range" Data Type, *AGU, Fall Meeting.* G31A–05.

Emergeo Working Group, 2009. Evidence for surface rupture associated with the Mw 6.3 L'Aquila earthquake sequence of April 2009 (central Italy), *Terra Nova,* **22,** 43–51, doi:10.1111/j.1365-3121.2009.00915.x.

Falcucci, E. *et al*., 2009. The Paganica fault and surface coseismic ruptures caused by the 6 April 2009 earthquake (L'Aquila, Central Italy), *Seism. Res. Lett.,* **80**(6), doi:10.1785/gssrl.80.6.940.

Galli, P., Galadini, F. & Pantosti, D., 2008. Twenty years of paleoseismology in Italy, *Earth Sci. Rev.,* **88**(1–2), 89–117, doi:10.1016/j.earscirev.2008.01.001.

Mantenuto, S., 2008. Active deformation in the central-northern Apennines (Abruzzo and Umbria-Marche regions, Italy) through the analysis of GPS data, *PhD thesis*. University of Perugia.

Okada, Y., 1985. Surface deformation due to shear and tensile faults in a half-space, *Bull. seism. Soc. Am.,* **75,** 1135–1154.

Pino, N.A. & Di Luccio, F., 2009. Source complexity of the 6 April 2009 L'Aquila (central Italy) earthquake and its strongest aftershock revealed by elementary seismological analysis, *Geophys. Res. Lett.,* **36,** L23305, doi:10.1029/2009GL041331.

Pondrelli, S., Salimbeni, S., Morelli, A., Ekström, G., Olivieri, M. & Boschi, E., 2009. Seismic moment tensors of the April 2009, L'Aquila (Central Italy), earthquake sequence, *Geophys. J. Int.,* **180**(1), 238–242, doi:10.1111/j.1365-246X.2009.04418.x.

Press, W.H., Teukolsky, S.A., Vetterling, W.T. & Flannery, B.P., 1992. *Numerical Recipes in C: The Art of Scientific Computing,* 2nd edn, Cambridge University Press, Cambridge.

Roberts, G. & Michetti, A.M., 2004. Spatial and temporal variations in growth rate along active normal fault systems: an example from The Lazio Abruzzo Apennines, central Italy, *J. Struct. Geol.,* **26,** 339–376, doi:10.1016/S0191-8141(03)00103-2.

Walters, R.J. *et al*., 2009. The 2009 L' Aquila Earthquake (Central Italy): a source mechanism and implications for seismic hazard, *Geophys. Res. Lett.,* **36**(L17312), doi:10.1029/2009GL039337.

SUPPORTING INFORMATION

Additional Supporting Information may be found in the online version of this article:

Figure S1. Time-series of continuous GPS with best-fitting exponential decay functions (see main text for details). The horizontal axes represent time (days) after the main shock (April 6th). The vertical axes represent displacements in mm. The vertical dashed lines indicate the time of the earthquake (blue) and the green lines 60 d afterward.

Figure S2. Trade-offs between the model parameters of the uniform-slip dislocation model obtained by applying the best-fitting technique to a large number of synthetic data sets, each one derived from adding synthetic realizations of data noise to the actual data set. The bottom row (histograms) shows the a posteriori distribution of the model parameters (the red dashed lines bracket the 95 per cent individual confidence intervals, while the green lines show the optimal parameter values). The other rows (scatter plots) represent the correlations between parameter pairs.

Figure S3. Resolution tests for coseismic (a,b) and post-seismic (c,d) slip distributions. Left-hand panels: input slip and synthetic displacements used in the inversion. Right-hand panels: estimated slip and predicted displacements. The blue vectors represent the horizontal displacements, while the green vectors the vertical displacements (error ellipses at 95 per cent C.I.). Note the different colour scale for coseismic and post-seismic slip distributions. A checkerboard test (a) highlights the poor resolution at depth. Slip in the shallower part is relatively well resolved. The slip (b) that would be estimated from an along-strike variable slip distribution. These tests show that the coseismic data have a limited resolution in the deepest part of the fault, that improves in the shallower parts. Post-seismic resolution test (c) of deep versus shallow afterslip. Specific slip configuration (d) in which the slip is imposed in the deepest, shallowest and intermediate portions. The different patches are recovered, showing that the post-seismic data set is able to resolve this particular slip distribution. Both solutions, however result in a significant smearing of the input model, in particular at depth.

Figure S4. Trade-off curves between fault-slip roughness and misfit function for coseismic (a) and post-seismic (b) slip distributions. The appropriate value of k is taken from where the misfit stops decreasing strongly with increasing slip roughness. The arrows mark the picked roughness for our final solution.

Table S1. Coseismic offsets of continuous GPS sites. A_e, A_n, A_u are east, north and vertical coseismic displacements (in mm) and associated 1σ uncertainties S_e, S_n and S_u.

Table S2. Coseismic offsets of survey-style GPS sites. A_e, A_n and A_u are east, north and vertical coseismic displacements (in mm) and associated 1σ uncertainties S_e, S_n and S_u.

Table S3. East, north and vertical cumulated 60 d post-seismic displacements (in mm) of continuous GPS sites P_e, P_n and P_u calculated using the exponential function $P_i = B_i\,[1 - \exp(-60.0/d_c)]$ and associated 1σ uncertainties S_e, S_n and S_u.

Table S4. East, north and vertical cumulated 60 d post-seismic displacements (in mm) of survey-style GPS sites P_e, P_n and P_u calculated using the exponential function $P_i = B_i\,[1 - \exp(-60.0/d_c)]$ and associated 1σ uncertainties S_e, S_n and S_u.

Table S5. Coefficients (in days) of the exponential post-seismic decay function of CGPS stations.

Table S6. Coefficients (in days) of the exponential post-seismic decay function of survey-style GPS stations.

Table S7. Source parameters of the 2009 April 6 L'Aquila earthquake. Values in parenthesis represent the individual 95 per cent confidence intervals determined using a Monte Carlo method (Fig. S2).

Please note: Wiley-Blackwell are not responsible for the content or functionality of any supporting materials supplied by the authors. Any queries (other than missing material) should be directed to the corresponding author for the article.